Journal of Volcanology and Geothermal Research 190 (2010) 337–352

Contents lists available at ScienceDirect

Journal of Volcanology and Geothermal Research

journal homepage: www.elsevier.com/locate/jvolgeores

Simulations of tephra dispersal from the 1991 explosive eruptions of Hudson volcano, Chile

David J. Kratzmann [a,*], Steven N. Carey [a], Julie Fero [a], Roberto A. Scasso [b], Jose-Antonio Naranjo [c]

[a] Graduate School of Oceanography, Univ. of Rhode Island, South Ferry Rd., Narragansett, RI, 02882, United States
[b] Departamento de Geología, Facultad de Ciencias Exactas y Naturales, Universidad de Buenos Aires, Ciudad Universitaria Pab. II, 1428, Buenos Aires, Argentina
[c] Servicio Nacional de Geología y Minería, Casilla, 10465 Santiago, Chile

ARTICLE INFO

Article history:
Received 9 July 2009
Accepted 19 November 2009
Available online 4 December 2009

Keywords:
Hudson volcano
PUFF simulations
Southern Volcanic Zone
tephra dispersal
tropospheric transport
wandering plume

ABSTRACT

The 1991 explosive eruptions of Hudson volcano in southern Chile produced 2.7 km^3 (dense rock equivalent) of basalt and trachyandesite tephra during the period August 8–15. The initial basaltic phase (phase I, August 8–9) produced a maximum column height of 12 km above sea level (ASL) and tephra fallout was directed to the north and northeast by the prevailing winds. The paroxysmal trachyandesitic phase (phase II, August 12–15) involved at least three separate events with a maximum ~18-km-high (ASL) eruption column inferred from satellite temperature data. During the initial 24 h of this phase the plume was advected almost directly south, before swinging towards the east as the wind changed direction. The plume was ultimately directed to the southeast and stayed relatively fixed at this bearing for the remainder of the eruption. These temporal variations in the main dispersal direction during the earlier stages of the phase II eruption produced a much wider overall deposit than would be expected from a plume with a relatively fixed transport direction (e.g., latter stages of phase II).

The Lagrangian ash tracking model PUFF was utilized to simulate the 1991 explosive eruptions and was able to successfully reproduce the aerial distribution and temporal evolution of the plumes. The optimal agreement between the observed and simulated plumes occurs when the highest concentration of ash particles coincides with the tropopause, a height that is typically lower than the maximum observed column heights for the 1991 eruptions. Gravitational settling of the laterally spreading umbrella region (e.g., Pinatubo 1991) may result in the concentration of ash at this level. This may account for differences in column height estimates between ground- or satellite-based and lithic-based models.

The plume associated with the paroxysmal phase (August 12–15, 1991) produced a multilayered deposit composed of alternating layers of fine ash and pumice lapilli. The highly stratified nature of the fall deposit is likely the result of multiple eruptive events coupled with a time varying wind field. A strongly changing wind direction that occurred during the earlier stages of the paroxysmal eruption could have produced variations in the dominant grain size being deposited between fine ash and pumice lapilli during individual eruptive sequences.

1. Introduction

Analysis of recent explosive eruptions has benefited from monitoring using advanced satellite instrumentation such as the Advanced Very High Resolution Radiometer (AVHRR), Total Ozone Mapping Spectrometer (TOMS), Moderate Resolution Imaging Spectroradiometer (MODIS), and Geostationary Operational Environmental Satellite (GOES) (e.g., Holasek and Rose, 1983; Rose, 2003; Tupper et al., 2004; Webley et al., 2009; Fero et al., 2009). AVHRR and TOMS data enable both the detection of ash and sulfur dioxide (SO_2) clouds from explosive events (e.g., Constantine et al., 2000; Webley et al., 2009) and the estimation of eruption column heights (e.g., Matson, 1984; Woods and Self, 1992; Tupper et al., 2004). Simulations of tephra dispersal from well-documented historic explosive eruptions can also be used to assess important source parameters such as eruption column height and downwind plume evolution. PUFF is a Lagrangian dispersal model that enables the tracking of ash particles from small to intermediate sized explosive eruptions and is used primarily for the mitigation of hazards to aircraft from volcanic ash plumes (Searcy et al., 1988). Previous simulations of explosive eruptions using PUFF have been limited to relatively small magnitude events that inject particles to tropospheric altitudes (e.g., Mt. Spurr 1991 [Searcy et al., 1988]; Mt. Etna 1998 [Aloisi et al., 2002]). Recent work has successfully applied PUFF to modeling larger, multi-phase events that extend into the stratosphere, such as the 1980 eruption of Mt. St. Helens (e.g., Fero et al., 2008) and the 1991 eruption of Mt. Pinatubo (e.g., Fero et al., 2009).

* Corresponding author. Tel.: +1 401 874 6254; fax: +1 401 874 6811.
E-mail address: davidk@gso.uri.edu (D.J. Kratzmann).

0377-0273/$ – see front matter © 2009 Elsevier B.V. All rights reserved.
doi:10.1016/j.jvolgeores.2009.11.021

The 1991 explosive eruptions of Hudson volcano in southern Chile injected ash into the stratosphere with the column height from the climactic phase reaching >18 km (Naranjo et al., 1993). An estimated 1.5 Mt of SO_2 (Doiron et al., 1991) was injected between 11 and 16 km altitude (Schoeberl et al., 1993). Approximately 2.7 km^3 (dense rock equivalent) of trachyandesite pyroclastic material was discharged during the event (Naranjo et al., 1993), with fallout of volcanic ash occurring over a large area to the north and east of the volcano extending across Argentina to the Atlantic Ocean (Scasso et al., 1994) (Fig. 1).

As a result of the very good documentation of both the atmospherically dispersed eruption plume (e.g., Constantine et al., 2000) and the subsequent tephra fall deposit (e.g., Naranjo et al., 1993; Scasso et al., 1994), the 1991 eruption of Hudson volcano provides an excellent opportunity to evaluate the relationship between these two eruption features. In particular, the event can be used to test the validity of models used to infer paleovolcanological parameters from ancient tephra fall deposits (e.g., Carey and Sparks, 1986). The PUFF ash dispersal model has been utilized to better constrain the eruption column height and plume evolution during the two phases of the Hudson eruption by comparing predicted dispersal patterns with satellite plume observations and ground-based tephra fall deposits. Refined eruption column heights from the PUFF simulations are then compared with inferred heights based on the distribution of pumice and lithic clasts in the fall deposit. A characteristic feature of the 1991 Hudson fall deposits is a highly stratified sequence with significant variations in grain size (Scasso et al., 1994). We explore how changing atmospheric conditions during an eruption can contribute to the origin of the highly stratified deposits and the potential problems in inferring eruption column height from such multilayered sequences based on the distribution of maximum lithic and pumice clasts.

2. Geologic setting and the 1991 eruptions of Hudson volcano

Hudson volcano (45.90°S, 72.97°W) is the southernmost volcano of the Andean Southern Volcanic Zone and has developed on ~30-km-thick crust, surrounded by exposures of the Patagonian Batholith (Kilian and Behrmann, 2003; Gutierrez et al., 2005. Tephra fall deposits surrounding Hudson Volcano record at least 12 Holocene–Recent explosive eruptions, with the most important being the August, 1991 eruptions, and two others dated at approximately 3600 and 6700 years before present (yrs BP [Stern, 1991; Naranjo and Stern, 1998]). Based on tephra records from postglacial lake sediments, Haberle and Lumley (1998) estimated that the frequency of major explosive eruptions from Hudson is of the order of 1 per 3800 calendar years.

The 1991 explosive eruptions of Hudson volcano involved two major phases, separated by a two-day period of relative quiescence, which generated compositionally and spatially distinct deposits. On August 8, 1991 (2220 UTC) the initial phase (phase I) of the Hudson eruption began with a phreatomagmatic event that produced a 7–10-km-high eruption column. Immediately following this initial explosion the eruption column reached ~12 km (Naranjo et al., 1993). In the early hours of August 9 (1991) lahars from the Huemules glacier descended the Huemules valley for the next 10 to 12 h (Bitschene and Fernandez, 1995). Basaltic lava flows erupted through a 4-km-long, north–northeast trending fissure in the northwestern corner of the caldera on August 9, 1991 (1430 UTC), producing a 7-km-high column of gas and minor ash. This initial phase of the eruption produced

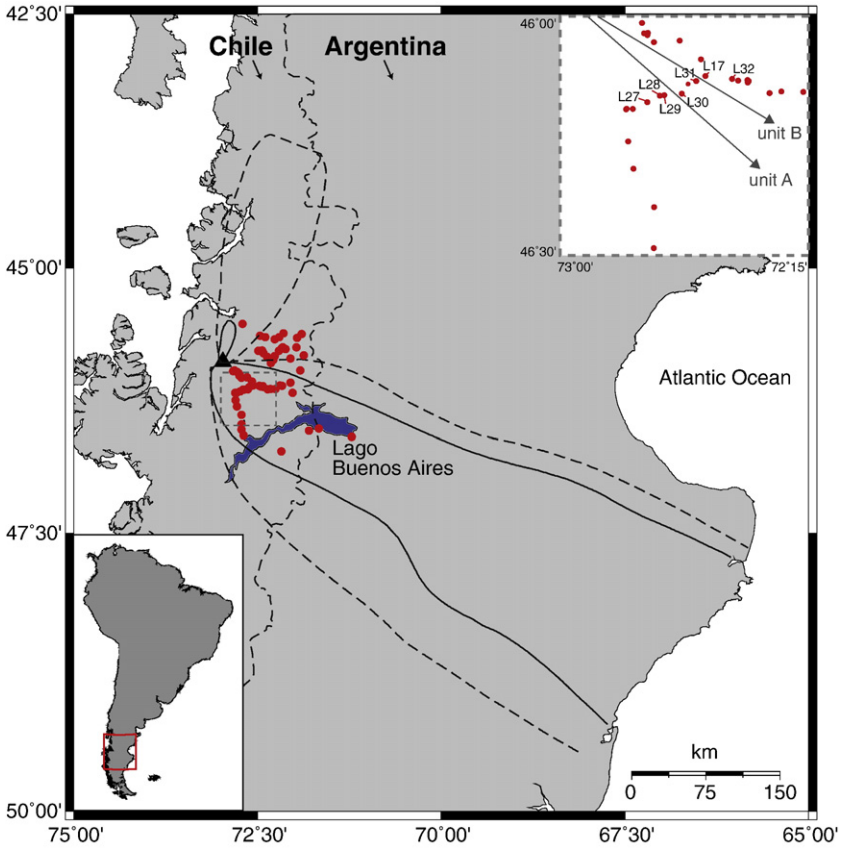

Fig. 1. Map showing the location of Hudson volcano (black filled triangle), sampling locations (red filled circles), and the 1.0 cm (solid black line) and 0.1 cm (dashed black line) isopachs for phases 1 (data from Naranjo et al., 1993) and phase II (data from Scasso et al., 1994) of the 1991 eruption. The locations of sampling sites used in Fig. 10 are shown in the top right inset map (gray dashed line in main map defines extent). Gray arrows are main dispersal axes for units A and B (PII). The main map extent is defined by the red box in the regional inset map (bottom left).

approximately 0.2 km^3 (bulk volume) of tephra deposited north–northeast of the vent by the prevailing winds (Fig. 1) (Naranjo et al., 1993; Scasso et al., 1994). Beginning on August 11, 1991 (1650 UTC) the second phase of the eruption (phase II) produced a 3-km-high column that was directed towards the south with limited fallout (phase II event 1, Fig. 2). The August 12, 1991 (1600 UTC) eruption produced a plinian-style eruption from a crater approximately 4 km to the south–southeast of the first crater (phase II event 2, Fig. 2). The

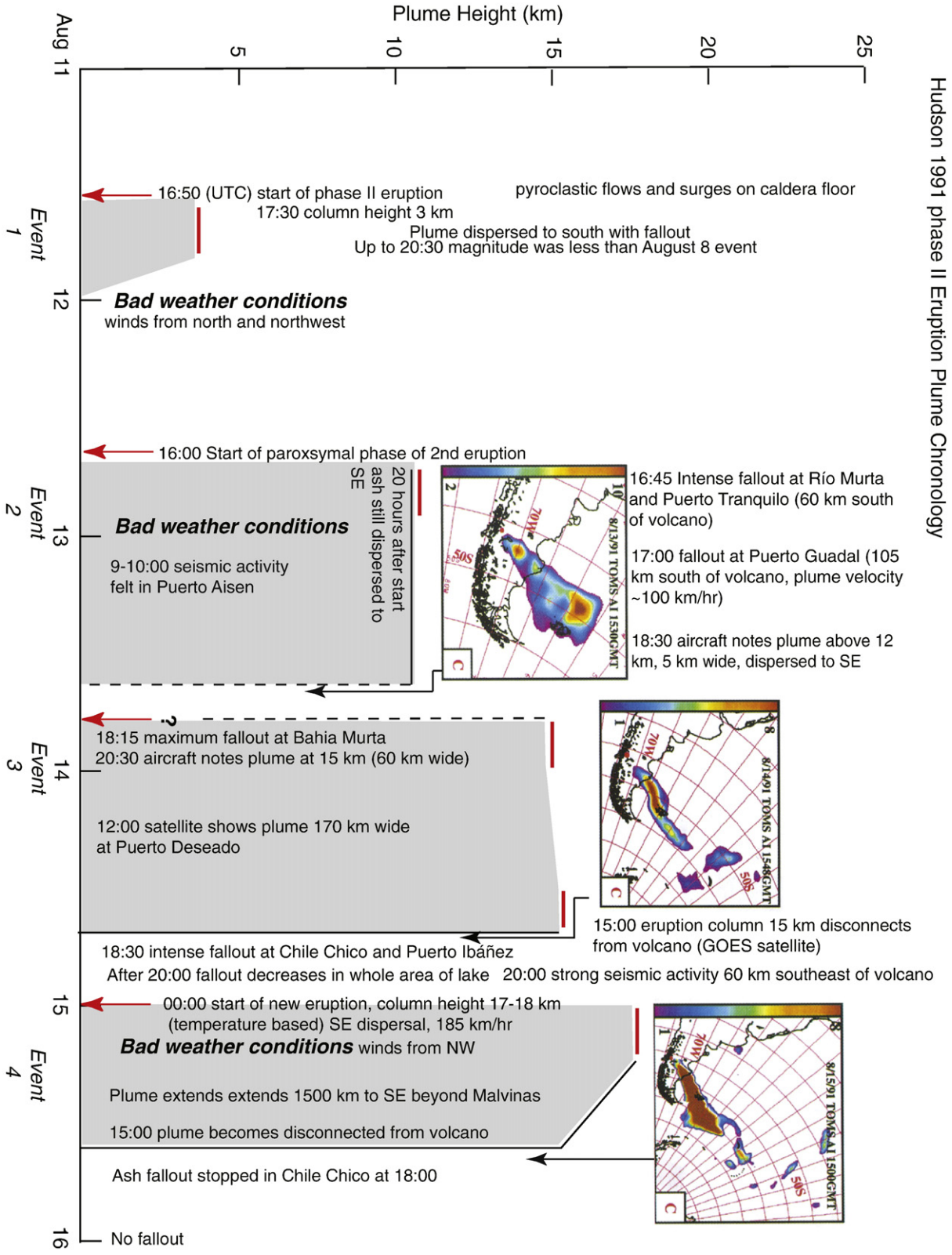

Fig. 2. Schematic representation of the plume chronology for phase II of the 1991 explosive eruptions of Hudson volcano. Filled gray boxes define the column heights and durations of eruptive events. Modified from Naranjo et al. (1993) and Scasso et al. (1994). TOMS AI images from Constantine et al. (2000).

column height during this event reached >10 km. Satellite imagery shows the plume disconnected from the volcano at 1530 UTC (August 13). On August 13, 1991 (2000 UTC) the eruption recommenced with the eruption column observed at ~15 km altitude (phase II event 3, Fig. 2). The ash plume from this event detached from the vent at 1500 (UTC) on August 14. The eruption recommenced again at approximately 0000 (UTC), generating an 18-km-high column (phase II event 4, Fig. 2), before finally stopping at 1500 (UTC) on August 15 (Naranjo et al., 1993; Scasso et al., 1994). Tephra from this paroxysmal phase of the eruption was directed southeast in an elongate plume and is reflected in the isopach distribution for the deposit (Fig. 1). Fall deposits extended to the Malvinas Islands ~1500 km to the south in a narrow band almost 370-km-wide that covered ~100,000 km^2 of southern Patagonia (Scasso et al., 1994).

3. PUFF simulations

The 1991 explosive eruptions at Hudson volcano were simulated using the PUFF ash tracking model (version 2.1.6). Initial PUFF input parameters such as eruption column height, column diameter, total number and distribution of ash particles, and grain size distribution can be controlled and systematically varied during simulations. The initial PUFF input parameters used were selected from available published observational data (e.g., Naranjo et al., 1993; Constantine et al., 2000) and previous applications of the PUFF model (e.g., Fero et al., 2008; Fero et al., 2009). Over the course of >300 simulations each parameter was systematically varied to identify the combination of variables required to reproduce the aerial distribution of ash particles that best matched the satellite imagery and fall deposits. The initial phase (phase I, August 8, 1991) and the paroxysmal phase (phase II, August 12–15, 1991) were modeled individually and then combined to produce a complete simulation of the eruption, following the methods of Fero et al. (2008). The open source software Generic Mapping Tools (GMT [Wessel and Smith, 1991]) was used to generate all maps.

A 40-year gridded, reanalysis data set from the National Center for Environmental Prediction (NCEP) was the primary wind field data utilized in the PUFF simulations and was obtained from the National Center of Atmospheric Research. The data set has a spatial resolution of 2.5° and a temporal resolution of 6 h, extending to 10 hPa (~30 km) with 17 levels of vertical resolution (Kalnay et al., 1996; Fero et al., 2008). Wind speeds in the Patagonia area are strong and generally increase with increasing altitude. On August 12 to 14, 1991 the wind speeds from the reanalysis data show an increase up to approximately 10–11 km altitude, then a decrease between 11–15 km, before increasing again beyond ~15 km. There is a large range in velocities at or about the tropopause (~11 km), from <10 ms^{-1} on August 8 (through 11) to >50 ms^{-1} on August 14. The wind speeds tend to converge on a range (65 to 75 ms^{-1}) at approximately 25 km altitude (Fig. 3). During the paroxysmal phase of the 1991 eruption the wind speeds at ~11 km altitude were at a peak velocity of >50 ms^{-1} on August 14, decreasing slightly to ~48 ms^{-1} on August 15 (Fig. 3). The velocities from the NCEP reanalysis data set agree with other reanalysis wind field data sets from the region (e.g., 50 ms^{-1} [Schoeberl et al., 1993]), and inferred from ash cloud movement (e.g., 51 ms^{-1} [Constantine et al., 2000]).

The PUFF input parameters were systematically varied over a range of values to identify the combination of factors required to best match the aerial distribution and temporal evolution of the 1991 ash clouds defined by satellite imagery (Table 1). Particle horizontal diffusivity was evaluated from 1000 m^2s^{-1} to 10,000 m^2s^{-1} at 1000 intervals, and from 10,000 m^2s^{-1} to 50,000 m^2s^{-1} at intervals of 10,000. These results indicate that above 10,000 m^2s^{-1}, horizontal diffusivity has a limited role in controlling plume location and thus was set at 5000 m^2s^{-1}, similar to values used in modeling the 1998 eruption of Mt. Etna (e.g., Aloisi et al., 2002). Vertical diffusivity was

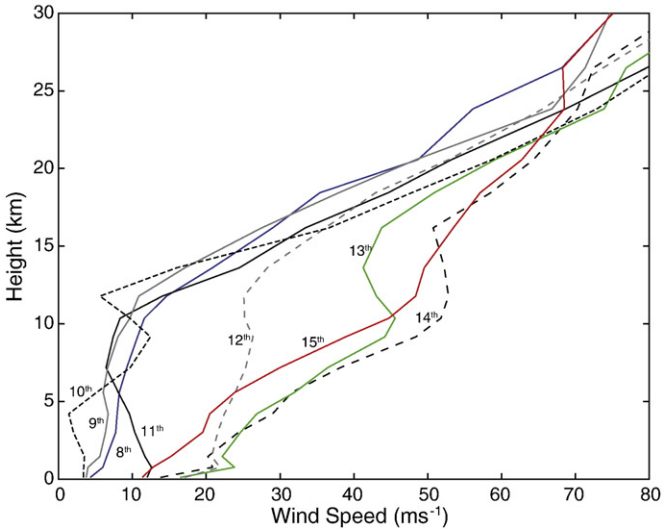

Fig. 3. Vertical profile of winds speeds (ms^{-1}) for the period August 8 to 15, 1991. Data extracted from the NCEP data set and plotted at discrete height intervals (data points not shown). Note the change from positive to negative slope for August 12 to 14 wind speeds that appears to coincide with the level of the tropopause. Most pronounced in the August 13 data.

set at 10 m^2s^{-1}, based on work by Fero et al. (2008, 2009). The total number of ash particles injected has limited impact on the aerial distribution of the simulated plumes. However, the total number of particles for each simulated event was adjusted to reflect inferred variations in ash loading visible in the satellite imagery (Table 2). Throughout the simulations a normal grain size (mean = 316 μm plus one standard deviation) and a Poisson vertical distribution of particles were used to best represent the umbrella shape of the plume. The vertical extent of particle injection (i.e., z-width) was varied at 1 km increments while holding the maximum column height at a fixed altitude (Table 1). The column height was also varied while holding the z-width static (2 km intervals, Table 1). Once emplaced in the atmosphere, the behavior of the ash is controlled by horizontal and vertical diffusion, and the particle-settling regime. Systematically varying the vertical extent of particle injection revealed that the simulations best match the observed plume evolution by setting the level of highest ash concentration (i.e., z-width) at or close to the tropopause at this latitude (10–14 km as defined by temperature data). This altitude range is similar to that identified by Schoeberl et al. (1993) during passive tracer modeling of the SO_2 cloud (11–16 km). Based on the cross-axis width of the isopach data in the proximal area of Hudson the column diameter was set at 5 km for phase I and 15 km for phase II. A subset of model parameters that best reproduced the aerial distribution of the plumes was selected from the test runs and utilized in producing the final eruption simulations (Table 2). Once completed, the aerial extent of the simulated plumes was compared directly to the satellite data processed by Constantine et al. (2000).

3.1. Satellite detection of the 1991 Hudson plumes

Volcanic ash clouds comprise varying amounts of volcanic gases, pyroclasts, aerosol particles, and water and gaseous species from the ambient atmosphere. It is the volcanogenic particles that enable satellite-based detection and tracking of ash clouds (Rose et al., 2000). The ash clouds associated with the 1991 explosive eruptions of Hudson volcano were thus able to be tracked by AVHRR and TOMS instruments onboard the NOAA-11 and -12 polar orbiting and NASA Nimbus-7 satellites respectively. The TOMS instrument is a UV spectrometer that measures the albedo of the sunlit Earth. Although originally designed to measure ozone (O_3), similarities between the

Table 1
Input parameters tested during PUFF simulations of the 1991 Hudson eruptions.

Parameter	1991 Phase I			1992 Phase II		
	Minimum input	Maximum input	Test interval	Minimum input	Maximum input	Test interval
Height (km)	7	12	1	10	30	2
Diameter (km)	10	20	10	20	30	10
Vertical spread (km)[1]	2	3	1	1	11	1
Number of ash particles	7000	12,000	2500	12,000	50,000	2000[2]
Horizontal diffusivity (m^2s^{-1})	2000	20,000	5000[3]	2000	20,000	5000[3]
Vertical diffusivity (m^2s^{-1})	10	20	10	10	20	10
Grain size[4]	−2.5	−4.5	1	−2.5	−4.5	1

(1) z-width (distance from top of column to point of highest concentration of ash particles).
(2) 12,000 to 20,000 at 2000 intervals and at 40,000 and 50,000.
(3) 2000 to 5000 at 1000 intervals; 5000 to 20,000 at 5000.
(4) Radius in meters ($r = 10^{-3.5}$) e.g., ash log mean of −3.5 is ~316 μm.

UV absorption spectra of O_3 and SO_2 enables the quantification of the latter from TOMS data (Krueger et al., 1995). The TOMS data can also provide an Aerosol Index (AI), a unitless scale determined by the spectral contrast between bands that are sensitive to suspended matter such as dust, smoke, and volcanic ash (Constantine et al., 2000; Tupper et al., 2004). The AI value approaches zero for water clouds and is positive for volcanic ash clouds and increases with optical depth (Tupper et al., 2004). The AVHRR instruments have two thermal infrared channels, bands 4 and 5, centered on 11 and 12 μm respectively. By subtracting band 5 brightness temperatures from band 4 brightness temperatures (e.g., Prata, 1989a,b) volcanic clouds can be distinguished from meteorological clouds. Volcanic clouds will have a negative brightness temperature difference (BTD), and meteorological clouds a positive BTD. This technique requires ash clouds to be translucent to upwelling thermal IR radiation, otherwise volcanic plumes are as opaque as meteorological clouds (Simpson et al., 2000). A review of space-borne instrumentation and their associated parameters can be found in Oppenheimer (1998) and Rose et al. (2000). Each satellite-based detection method has advantages and disadvantages that require their mutual use in an overlapping method depending on the environmental conditions at the time of the eruption (e.g., Constantine et al., 2000).

Some discrepancies between the aerial extent of the simulated plume and the actual ash cloud may be due to the various detection methods employed by the different instruments. For example, AVHRR data can be used for either opaque (i.e., band 4 at 10.6 μm) or translucent (i.e., BTD at 1–10 μm) ash clouds (Oppenheimer, 1998; Constantine et al., 2000; Tupper et al., 2004). Translucent ash clouds may not be detectable in AVHRR band 4 but will be definable in the BTD data. With respect to the 1991 eruption of Hudson, the total mass of fine ash (1–12 μm) determined from satellites (2.9×10^6 t [Constantine et al., 2000]) is much less than 1% of the total deposit (7.6×10^9 t [Scasso et al., 1994]). There may be an atmospherically suspended portion of the plume that is not 'visible' to the instruments. Also, the discrimination between volcanic ash clouds and water/ice clouds can be difficult when 1) there are many high meteorological clouds present, 2) the maximum column height is lower than the surrounding atmospheric clouds, and 3) if abundant ash–ice hydrometeors, which have the spectral signal of ash, are formed (Oppenheimer, 1998; Rose et al., 2000; Tupper et al., 2004). Furthermore, subjectivity associated with identifying the edges of ash clouds in satellite images depends to some extent on the interpretation of the user (e.g., Oppenheimer, 1998). Therefore the traced outlines, while useful for comparative purposes, may not necessarily provide an exact match between simulated and detected ash clouds.

3.2. Temporal evolution of the 1991 plumes

The initial phase of the 1991 eruption (phase I, August 8) produced a ~7–12-km-high column and the associated cloud was broadly dispersed to the north and northeast by the prevailing winds. By early on the morning of August 9 the cloud appeared to have narrowed and was primarily directed NNE to NE (Fig. 4a). However, the low ash content of this initial phase makes it difficult to define the boundaries of the cloud from satellite imagery (Constantine et al., 2000).

The spatial evolution of the plumes associated with the four events that occurred during paroxysmal phase of the 1991 eruption was quite complex. Ash from the ~3-km-high eruption column associated with the August 11 event (phase II event 1) was dispersed to the south without significant amounts of ash deposition (Naranjo et al., 1993). During the approximately 23-hour duration of the August 12 event (phase II event 2) the ash particles were transported almost directly

Table 2
Model parameters utilized during combined PUFF simulation of the 1991 Hudson eruption.

Eruption phase	Date	Event	Plume height (km)	Number of particles	Z-width (km)	H-width (km)	Horizontal diffusivity (m^2s^{-1})	Vertical diffusivity (m^2s^{-1})	Plume shape	Eruption duration (h)
I	8-Aug	n.a.	10	10,000	2	5	5000	10	P	12
	9-Aug	n.a.	7	5000	2	5	5000	10	P	12
II	11-Aug	1	3	5000	1	10	5000	10	P	7
	12-Aug	2	12	20,000	1	15	5000	10	P	23
	13-Aug	3	15	20,000	3	15	5000	10	P	20
	15-Aug	4	18	40,000	6	15	5000	10	P	15

n.a.: not assigned; P: Poisson distribution.

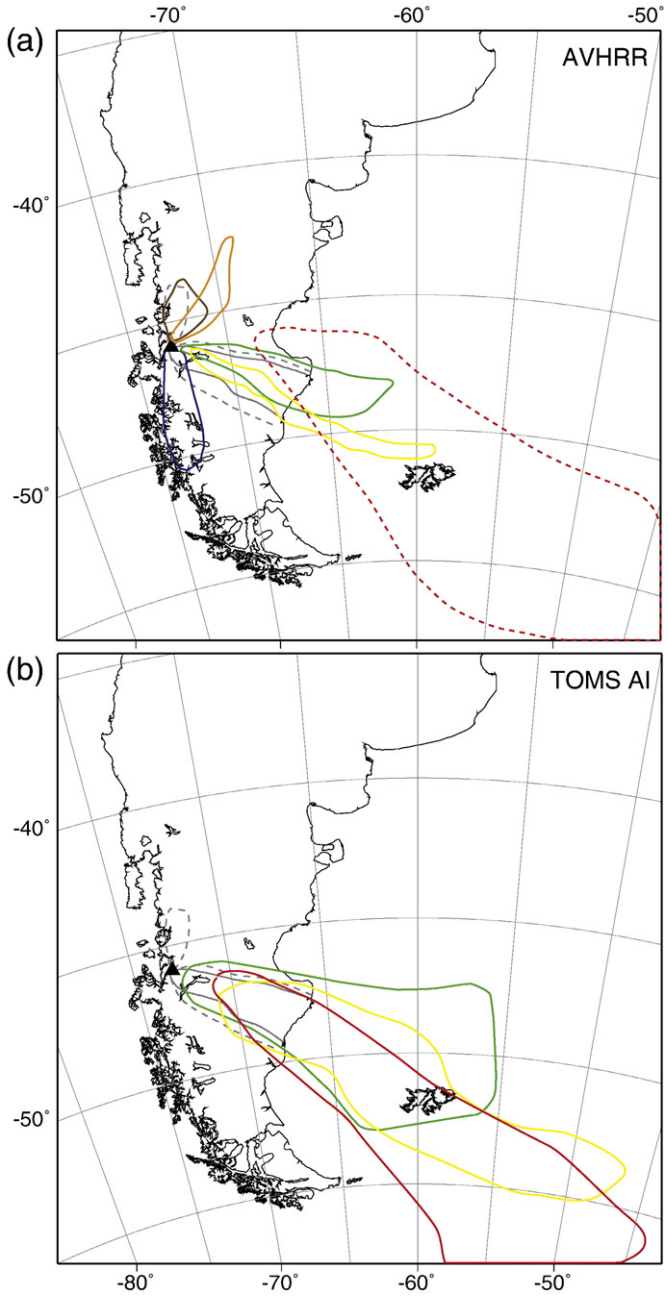

Fig. 4. Comparison of aerial extent and temporal evolution of the ash clouds from the 1991 explosive eruptions inferred from satellite imagery. (a) AVHRR symbology: August 9 at 0131 UTC (brown), August 9, 1427 (orange), August 12, 1902 (blue), August 13, 0214 (green), August 14, 0102 (yellow), August 15, 1300 (red). The red dashed line is the inferred outline (August 15) due to lack of clear signal in the AVHRR image. (b) TOMS AI symbology: August 13, 1130 UTC (green), August 14, 1148 (yellow), August 15, 1100 (red). 1 cm (gray solid line) and 0.1 cm (gray dashed line) fall deposit isopachs are also shown for comparison.

south, before swinging towards the east on August 13 as a result of the changing wind direction. Early on August 13 the wind has settled into a southeasterly direction that typifies the remainder of the eruption. The plumes associated with events 3 (August 13) and 4 (August 14) of the phase II eruption were quite narrow, showing little meridional dispersal, and were transported towards the southeast by strong winds. The overall southeast movement of the ash cloud from the latter events of the second phase is reflected in the AVHRR band 4 (Fig. 4a) and the TOMS AI imagery (Fig. 4b).

3.3. Phase I simulations (August 8–9, 1991)

PUFF simulations of phase I of the 1991 eruption reproduce the overall northward movement of the ash clouds associated with both the phreatomagmatic (August 8) and the fissure (August 9) events (see Supplementary animation, A1). The aerial extent of ash particles from the phreatomagmatic phase of the eruption has been distinguished in the AVHRR band 4 imagery by Constantine et al. (2000). The ash cloud was not visible in the AVHRR BTD images available (e.g., Constantine et al., 2000). Successful simulation of the plume is achieved by using a 10-km-high column with a 1 km z-width (Fig. 5a). The solid black line in Fig. 5 represents the most visible portion of the plume (from plate 1a of Constantine et al., 2000). The dashed black line represents the possible furthest extent of the plume or a meteorological cloud. If the column height is raised to 12 km, the predicted distribution of ash particles is much wider than the plume defined by Constantine et al. (2000) from the AVHRR band 4 imagery (Fig. 5b). Horizontal diffusivity has little impact on controlling the broadening visible in the simulated phase I plumes. The wider distribution most likely results from slight variations in the wind direction and speeds at these different altitudes. The simulated 12-km-high column height injects ash particles into higher altitude winds that trend east–northeast, and results in faster lateral (or horizontal) transport, and therefore a broader plume.

The aerial distribution of ash particles associated with the August 9 (1991) fissure eruption is best simulated with a 7 km column height and 1 km z-width. Under these conditions the narrowness of the plume is recreated, however the distribution of the simulated ash particles is slightly offset (to the west) from the plume margin to the satellite data (Fig. 5c). The simulated plume best matches the AVHRR band 4 image at 0100 (UTC) on August 10, 1991 (Fig. 5d).

In general, the simulations of the first phase of the 1991 eruption can successfully reproduce the distribution of the plumes, as distinguished by the satellite imagery processed by Constantine et al. (2000). The aerial extent of the simulated ash particles also encompasses the field defined by the fall deposit isopachs (Fig. 1). Phase I of the 1991 eruption is best reproduced using a slightly lower column height than reported for the phreatomagmatic event (i.e., 10 km versus 12 km), and the reported 7-km-high column for the subsequent fissure eruption.

3.4. Paroxysmal phase II simulations (August 12–15, 1991)

The paroxysmal phase of the 1991 eruption involved at least three (e.g., Scasso et al., 1994) and potentially four (this study) major eruptive events associated with well-developed plinian eruption columns. Published AVHRR and TOMS satellite data is available for certain times during the eruption sequence of August 12 to 15, 1991 (e.g., Constantine et al., 2000), and the aerial extent of the simulated plumes was visually compared to the ash clouds detected in these previously processed images.

3.4.1. August 11, 1991 (phase II event 1)

Simulations of the August 11, 1991 eruption (event 1), conducted with a 3-km-high column, show the plume being advected towards the south as a result of the prevailing winds. There is a minor change in the wind direction during this phase of the eruption, from west–southwest in the initial stage to south–southeast in the latter. When the plume from the August 11 simulation reaches approximately 55°S, the August 12 event 2 starts and both plumes move in a south–southeast direction. Although a relatively small event compared to the latter stages of the paroxysmal eruption, we have included the modeling results in the overall simulations for comparative purposes. See combined animation (Supplementary animation, A5) for a simulation of this event, which appears as southward-directed, blue

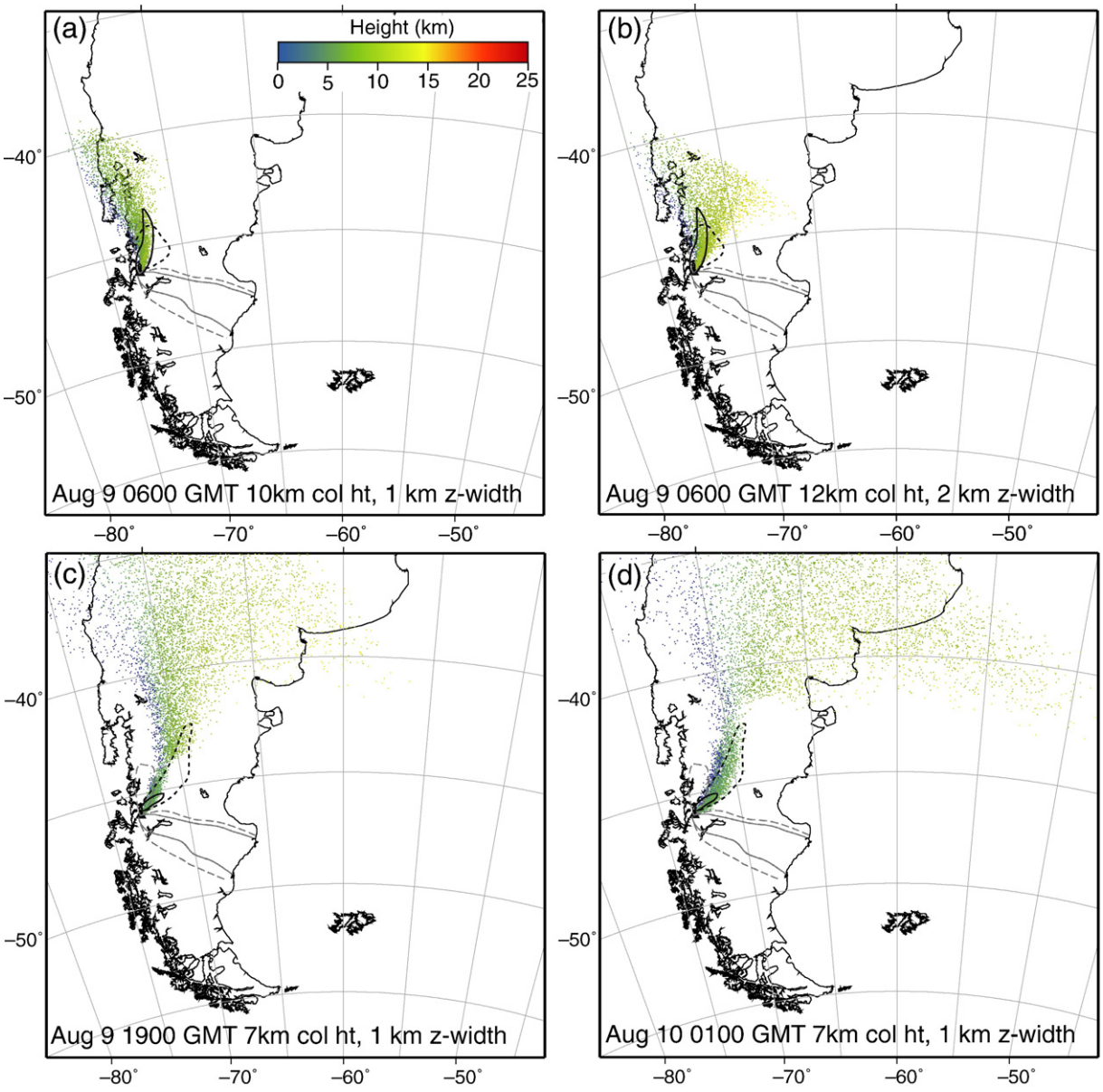

Fig. 5. Comparisons of the aerial extent of the simulated plume from phase I of the 1991 eruption (see Tables 2 and 3 for input parameters). Simulations from August 9 at 0600 (UTC) with (a) 10 km column, and (b) with 12 km column. (c) August 9, 1900 (UTC) with 7 km column. August 10, 0100 (UTC) with 7 km column height. Solid black line is plume outline of clearly visible ash cloud taken from satellite band 4 imagery (plate 1 of Constantine et al., 2000). The dashed black line is the potential extent of the plume (abundant meteorological clouds in the band 4 image make clear delineation difficult). Gray lines are isopachs (0.1 cm dashed and 1.0 cm solid). Ash particle height is denoted by color.

colored particles after the initial two events of phase I, and directly before the significantly larger August 12 event.

3.4.2. August 12–13, 1991 (phase II event 2)

The ash cloud associated with the start of the paroxysmal phase (1600 UTC August 12) of the eruption is initially directed towards the south by the prevailing winds. The southward dispersal of these ash particles can be effectively simulated with a range of eruption column heights up to 15 km and a range of z-width values that inject the highest concentration of particles at an altitude around 11 km (see Supplementary animation, A2). The simulated event matches the general shape of the plume boundary, but with some easterly displacement. Varying the horizontal diffusivity does not eliminate this eastward dislocation of the simulated plume. There may be atmospherically suspended ash in this location that is simply not being detected by the AVHRR BTD method. In addition, the simulation does not reproduce the southernmost extent of the plume shown in the AVHRR band 4 image (1902 UTC; Fig. 6a) until after 2200 UTC (Fig. 6b). The corresponding plume outline (red dashed [from Constantine et al., 2000] and black solid lines [this study]), taken from the AVHRR band 4 image (1902 UTC), is shown for comparison. The discrepancy between simulated and observed plume speeds would appear to be related to wind speed. The simulated plume is traveling in a southward direction at approximately 20 ms^{-1} whereas AVHRR band 4 image-based estimations suggest speeds great than 40 ms^{-1}. The average wind speed on August 12 only reaches 40 ms^{-1} at ~15 km altitude. Therefore, an eruption column height greater than 15 km is required for the plume to reach the southernmost extent shown in the satellite image (e.g., Fig. 6a [by 1900 UTC]). However, simulations involving eruption columns up to >15-km-high do not reproduce the orientation of plume as seen in the satellite data (no meridional extension). In fact, a much broader plume is generated as ash is advected to the east (zonal extension) owing to the predominantly southeast direction of the zonal component of the

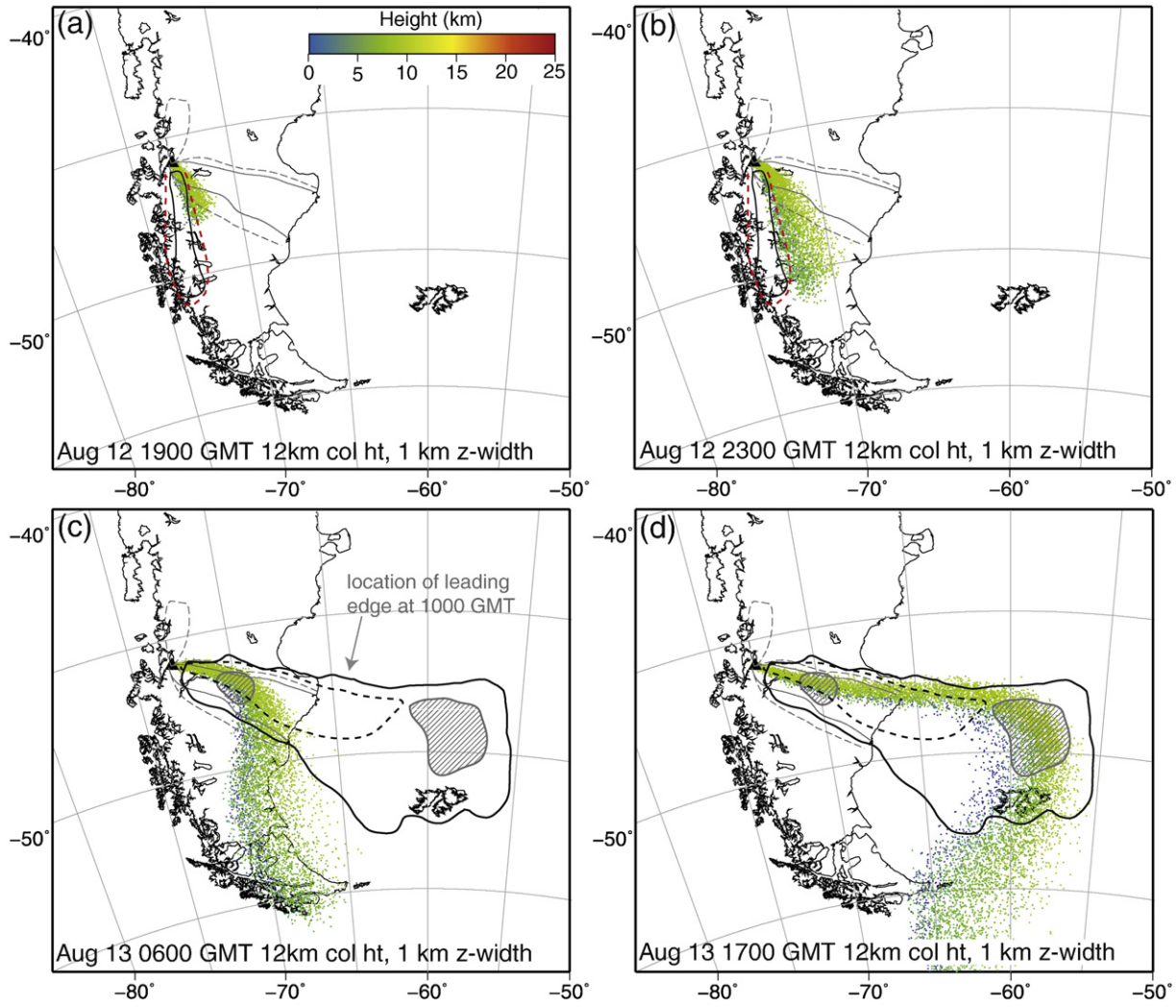

Fig. 6. Comparisons of the aerial extent of the simulated plume from event 2 of the phase II 1991 eruption, from August 12 (a and b) to August 13 (c and d). Dashed red line in (a) and (b) is plume outline from AVHRR image as traced by Constantine et al. (2000). Solid black line is trace from this study. In panels (c) and (d), dashed black line is AVHRR band 4 trace at 0614 (UTC) and solid black line is TOMS AI trace at 1500 (UTC). The arrow (c) denotes the northern most extent of the simulated plume at 1000 (UTC). Gray lined areas in (c) and (d) represent zones of high ash concentration visible within TOMS AI images. Ash particle height is denoted by color.

wind above 15 km altitude. The spatial discrepancy between the simulated and observed plumes may stem from the use of the reanalysis wind field, which averages data over large areas (i.e., 2.5° spatial resolution) and may not successfully replicate the localized, kilometer-scale winds.

At approximately 0000 UTC on August 13 (1991) the wind speed increases to ~40 ms^{-1} and the direction shifts from northerly to westerly (Fig. 3). This major change (from August 12 to 13) causes the plume to sweep from an initial southerly direction to a more easterly one before finally settling into a southeasterly trend. At 0600 (UTC) on August 13 the simulation has started to disperse ash particles eastward and the aerial distribution mirrors that of the plume outline from the majority of the terrestrial portion of the AVHRR band 4 image (Fig. 6c [see Supplementary animation, A2]). The simulation does not completely fill the seaward portion of the TOMS AI plume outline (solid black line, 1500 UTC), until closer to 1600 UTC (Fig. 6d).

The relatively strong winds (~20 ms^{-1} August 12 and ~40 ms^{-1} August 13) during event 2 of phase II result in a narrow plume in the proximal to medial regions east of the volcano. The narrow simulated plume does not match the width of the fall deposit as delineated by the total deposit isopachs (Fig. 6). However, changes in wind direction during the event distort the plume like a wet noodle resulting in fall deposition that wanders in the meridional direction (i.e., north–south orientation). The net effect of this "wandering plume" is to widen the crosswind depositional area relative to any instantaneous image of the plume position based on satellite images or simulations (Fig. 6).

There are two interesting features visible within the TOMS AI image from August 13, 1991 (1530 UTC). First, there are two zones of high ash concentration within the defined plume (Fig. 6c). The zone of high particle concentration to the east (over the Atlantic Ocean) may be ash from the beginning of the August 12 event, whereas the other zone of high concentration closest to the volcano may represent the final phase of event 2, prior to disconnection from the volcano. Second, the plume is more pronounced and much broader in meridional extent in the TOMS AI image relative to the AVHRR BTD image and the AVHRR band 4 image (plate 4a, 4b and 4c of Constantine et al. (2000) respectively). This discrepancy may be an artifact of the temporal separation of the two satellite images, the satellite orbits are ~9 h apart. The TOMS AI image may simply reflect an extra ~9 h of meridional expansion of the plume. Alternatively, the difference in meridional extent may result from the different ash detection techniques employed by the two instruments. The TOMS AI instrument, which relies on the scattering of solar energy to detect ash particles, may be detecting the true shape and extent of the plume. In contrast, ash detection by the AVHRR instrument is based on

scattering of upward-radiating thermal energy. If the edges of the plume are translucent (having a low optical depth) it may not be detectable in AVHRR band 4 alone but will be in AVHRR BTD. However, even though the signal is patchy and discontinuous relative to the AVHRR band 4, the plume is identifiable in the AVHRR BTD imagery (plates 4a and 4b of Constantine et al., 2000), Large amounts of moisture present within the ash cloud (e.g., Rose et al., 2000; Tupper et al., 2004) could account for the weaker plume signal in the BTD image (e.g., plate 4a of Constantine et al., 2000) and may explain the narrowness of the plume outline in the AVHRR band 4 image relative to the TOMS AI image (Fig. 6c and d).

3.4.3. August 13–14, 1991 (phase II event 3)

PUFF simulations of the August 13–14 event 3 were carried out starting at 2000 UTC (August 13, 1991) using the observed eruption column height of 15 km (Table 2; see Supplementary animation, A3). The simulated plume successfully reproduces the southeast direction and propagation speed as defined by the AVHRR band 4 image (0502 UTC) on August 14 (Fig. 7a). While the simulation can reproduce the initial narrowness of the plume, as time progresses the leading edge of the plume becomes much wider than recorded by the AVHRR band 4 image (Fig. 7a). Reducing the horizontal diffusivity does not substantially narrow the leading edge of the plume. Increasing the horizontal diffusivity above 10,000 m^2s^{-1} results in a broader leading edge to the ash cloud. Increasing the eruption column height (>16 km), while maintaining the narrowness of the initial plume, results in a more northward dispersal of ash particles. Similarly, decreasing the column height (<13 km) shifts the plume slightly more towards the south. In this case, translucent edges of the ash cloud may account for the narrowness of the plume in the AVHRR band 4 image. Although highly scattered, the ash cloud is detectable in the BTD image and is much broader than the narrow, continuous plume recorded by the band 4 image.

The z-width can be varied between 3 and 4 km (at 15 km column height) for event 3, such that the majority of ash is injected at or near the tropopause, to successfully reproduce the aerial distribution of the plume. Beyond this range there is much more meridional dispersal of the plume. Unlike event 2 of the phase II eruption sequence, the wind direction during event 3 was established in a southeasterly direction and remained relatively constant. Both the simulated plume and the outline from the AVHRR band 4 image (0502 UTC) are located within, and confined to the area defined by, the 1.0 cm isopach of the phase II fall deposit (Fig. 7). The width of the plume from the satellite imagery also closely matches the northern and southern extents of the 0.1 cm

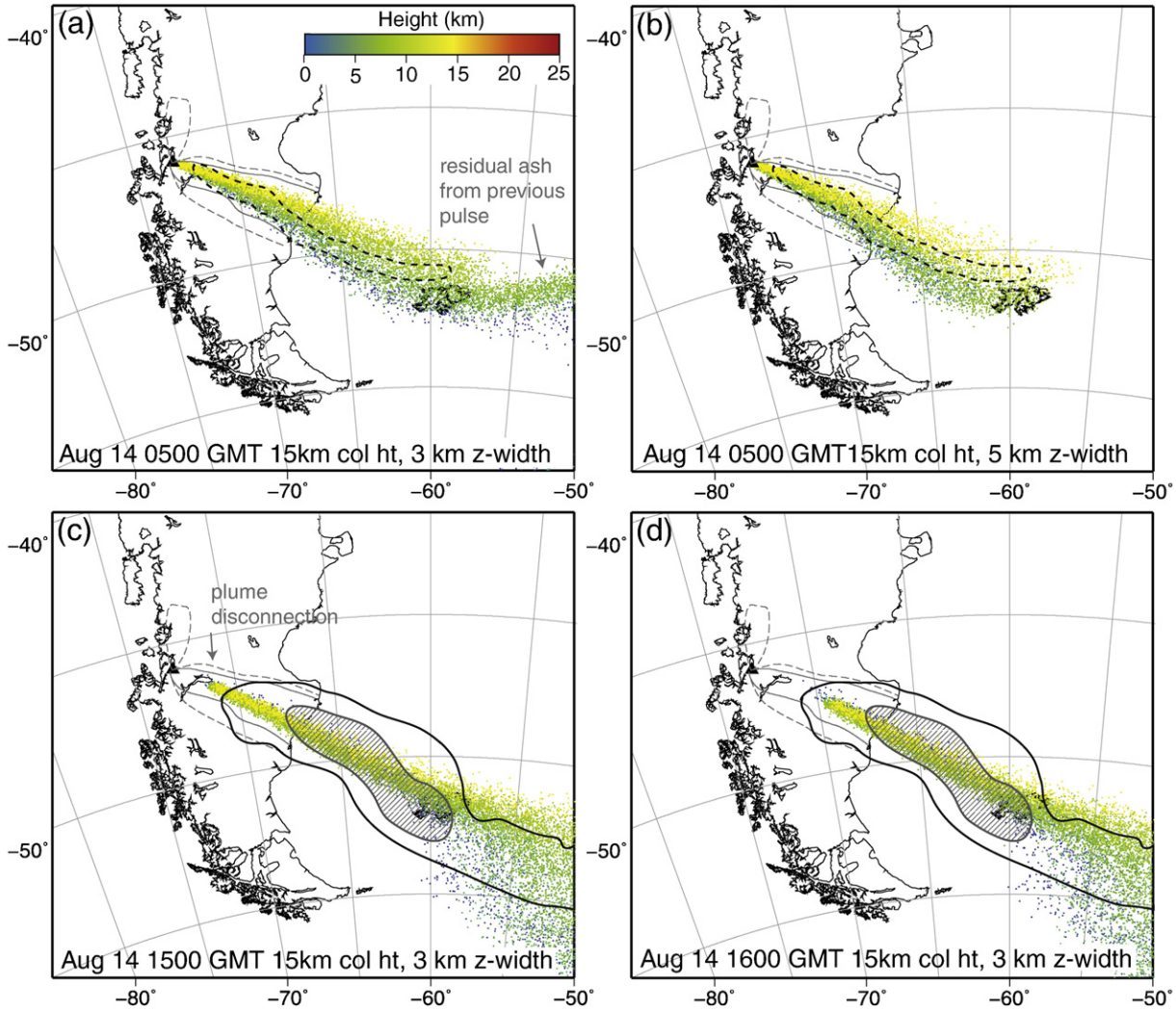

Fig. 7. Distribution of simulated ash particles from the August 13–14 (1991) event 3. (a) and (b) have varying z-width (3 and 5 km respectively). (c) and (d) show plume disconnecting and moving away from the edifice. Dashed black line (a and b) is plume outline from AVHRR band 4 image (0502 UTC), solid black line (c and d) is plume trace from TOMS AI image (1548 UTC). Gray lined fields in (c) and (d) represent areas of high ash concentration visible within TOMS AI images. Particles scattered throughout the eastern portion of panel (a) are residual ash from previous event. Ash particle height is denoted by color.

isopach for the overall deposit (Fig. 7). The simulated plume is narrower than shown in the TOMS AI imagery but is still confined within the 1.0 cm isopach (Fig. 7).

3.4.4. August 14–15, 1991 (phase II event 4)

Simulations of the aerial distribution of ash particles from the August 14 to 15 event 4 closely match the plume outline (from the TOMS AI imagery) and successfully reproduce the southern extension of the plume using a variety of column heights ranging from 15 to 22 km (Fig. 8; see Supplementary animation, A4). The simulations indicate that the best matches occur when the z-width was set such that the majority of ash particles were injected at, or slightly above, the tropopause (~11 km). This can explain why such a range in column heights can successfully replicate the aerial distribution of the plume. For example, a 16-km-high column with a 4 km z-width (Fig. 8a), an 18-km-high column with a 6 km z-width (Fig. 8c), and a 22-km-high column (11 km z-width) all produce similar results. An 18-km-high column with 3 km z-width injects the highest concentration of ash particles above the tropopause and produces a more northerly extent for the simulated plume (Fig. 8b). The PUFF model has a maximum z-width distance that can be set during simulations (i.e., 11 km) and this imposes an upper limit of control that can be exerted through the manipulation of the z-width value. Therefore, simulations conducted with a 25-km-high eruption column and the maximum z-width allowable by PUFF will inject the majority of ash particles at 14 km altitude, slightly above the tropopause, and produce a plume with a more northerly extent than observed during the eruption (Fig. 9). It follows that a 25-km-high eruption column with the highest concentration ash particles injected at or around the tropopause could also successfully match the aerial distribution of the plume if the z-width could be set to 14 km.

The TOMS AI image suggests much higher ash concentrations within the event 4 plume compared to the earlier events (e.g., plate 6c of Constantine et al., 2000). Relative particle concentration is designated by color, with the highest aerosol index represented by red, and blue being the lowest (Fig. 2). Interestingly, there is no significant ash cloud clearly evident in the AVHRR images (plates 6a and b of Constantine et al., 2000). The relatively high ash concentration (i.e., optically thick) may have rendered the plume invisible to the sensor by effectively blocking transmission of all ash-scattered thermal energy (e.g., Constantine et al., 2000). Alternatively, effective detection of the ash cloud by may have been obscured by the presence of significant amounts of meteorological clouds (visible in plate 6b of Constantine et al., 2000).

At the end of this event the plume disconnects from the volcano, and the simulated dispersal of the ash cloud closely matches the TOMS AI plume outline (Fig. 8d). As with the previous event of the phase II sequence (i.e., 3), the width of the simulated plume closely matches the northern and southern extents of the 1.0 cm isopach of the fall deposit (Fig. 8).

In summary, variations in eruption column height and z-width displayed a strong influence on plume shape and evolution throughout

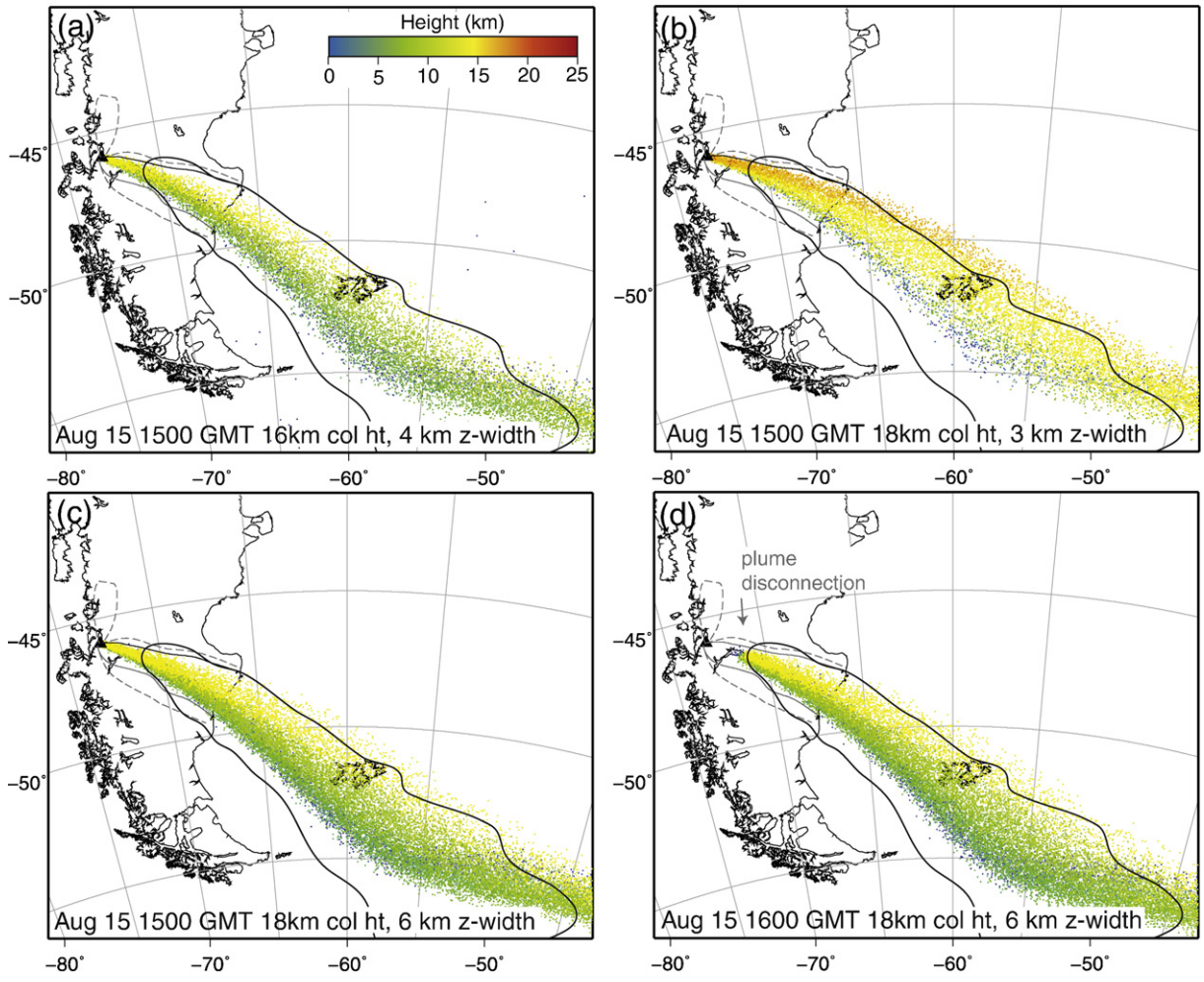

Fig. 8. Comparisons of the aerial extent of the simulated plume from event 4 (August 14–15) of the second phase of the 1991 eruption. Panels (a) and (b) show the influence column height has on particle distribution. Variations in z-width are shown in (b) and (c). Plume disconnection is shown in panel (d). Ash particle height is denoted by color.

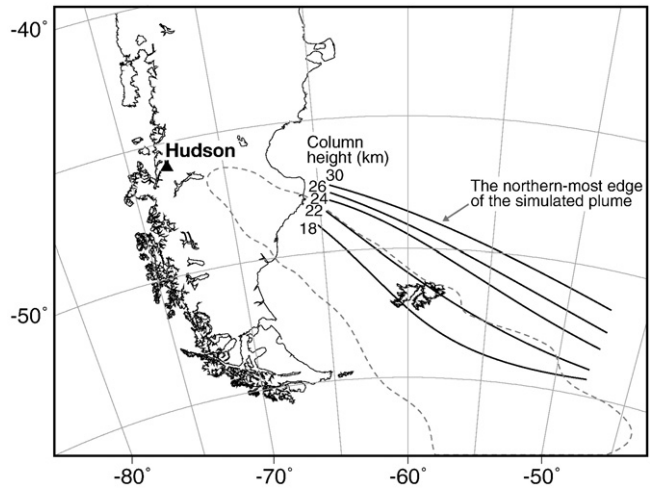

Fig. 9. The influence of varying column height with a fixed z-width on the northernmost edge (solid black line) of the simulated ash cloud from event 4 (August 14–15, 1991). With increasing column height the position of the northernmost extent of the plume edge shifts towards the north. Dashed black line represents the plume outline as distinguished from the AVHRR imagery. The zone of ash concentration (z-width) is set at the PUFF upper limit (11 km). For example, the 30 km column has the zone of ash concentration at 19 km. For the 18-km-high column, the highest ash concentration is located at approximately 7 km.

the course of simulating the 1991 eruptions of Hudson volcano. The optimal agreement between the simulations and satellite observations occurs when ash is transported at or around the tropopause (~11 km). Therefore, to ensure that the injection point for the highest concentration of ash particles in the column remains at or close to the tropopause, the z-width must be systematically increased as a function of increasing column height. This suggests that several combinations of column height and z-width extents can produce similar results. The combined simulations can successfully reproduce the aerial distribution and temporal evolution of the plumes from the 1991 events, and closely match the distribution of the fall deposits (see Supplementary animation, A5).

4. Stratigraphy of the 1991 phase II fall deposits

The phase II 1991 Hudson tephra fall deposits were studied at 71 locations in Chile and Argentina during fieldwork in 2005 and 2006. At each site the deposit thickness and stratigraphic sequence was recorded, and maximum pumice and lithics measured. An examination of in situ phase I fall deposits was not possible as they are no longer preserved in the field. A distinctive feature of the phase II fall deposit is a highly stratified sequence with significant variations in grain size that are traceable up to 50 km from source. Deposits are composed of alternating units of pale-gray fine ash, and gray coarse lapilli, with sharp contacts between units. Glassy tephra range from pale gray/white tube pumice to dark brown/black, blocky, poorly vesicular shards (Scasso and Carey, 2005). Stratigraphic columns (Fig. 10) are presented for each of the sampling locations that transect the main dispersal axis of the paroxysmal phase II fall deposit (Fig. 1 inset map).

Because of limitations in nighttime data collection and bad weather conditions during the 1991 eruptions, the observations and satellite imagery of the eruption plumes are limited in scope and incomplete (e.g., Constantine et al., 2000). The summary of the eruption chronology shown in Fig. 2 identifies three main eruptive events (2–4) during phase II of the eruption (Naranjo et al., 1993; Scasso et al., 1994; Constantine et al., 2000). However, the stratigraphy of the fall deposit records eruptive events, fluctuations in column height, and changes in wind direction in greater detail than observed during the eruption. Stratigraphic correlations of individual subunits between sampling localities have been made based on similarities in characteristics such as grading, clast size, sorting, and suggest at least four events occurred during the paroxysmal phase of the eruption (Fig. 10). Correlation of the uppermost fall sequence is difficult because of potential post-depositional erosion and reworking since the eruption in 1991. However, section locations were selected in flat areas away from significant slopes where runoff would lead to significant erosion. In addition, the transect in Fig. 10 is in an area where the grain size of the deposit was quite coarse ($\gg$1 mm) and therefore not particularly susceptible to aeolian reworking.

The main dispersal axes for the correlated units vary slightly in orientation: unit A trends approximately ~138°E, unit B, ~130°E, unit C and D at ~133°E. The uppermost coarse layer of the deposit trends ~135°. The main dispersal axes for units A and B show some evidence for varying wind direction (Fig. 1 inset). The variation in direction of these axes explains why the 0.1 cm isopach for the total deposit is much wider than any individual correlated unit or simulated plume. The thickest part of the deposit for units A, B, and D is found at sampling locale 31, whereas thickness maximum for unit C occurs at locale 29 (Figs. 1 and 10).

4.1. Stratigraphic complexity

The stratigraphic correlation diagram highlights the complexity of the deposits associated with the early stages of the paroxysmal phase of the eruption (Fig. 10). In some instances (e.g., localities 28, 29, 30, and 17) the lower 50% of the deposit is characterized by frequently alternating layers of fine ash and pumice lapilli. The upper portion of the stratigraphy is less complex, being predominantly composed of pumice lapilli fall deposits. The complexity visible in the base of the deposit could be the result of a change in eruption style from plinian to phreatoplinian, or fallout of fine ash during periods of quiescence or reduced eruption intensity (e.g., Walker, 1981; Carey and Sigurdsson, 1987; Scasso et al., 1994). Alternatively, the multilayered stratigraphy may result from a highly varying wind direction. On August 12, 1991 the strongly shifting wind orientation directed the plume across what was eventually the main dispersal axis of the unit twice during the 23-hour event. As the wind direction changed and pushed the plume back and forth across the main dispersal axis (trends ~138°E), the dominant grain size being deposited may have changed resulting in alternating fine and coarse layers. Cross-plume variations in grain size characteristics may arise from preferential transport of the fine ash component of a plume (e.g., Mt. St. Helens [Sarna-Wojcicki et al., 1981]). Complexity within tephra fall distribution patterns due to changing wind direction has also been identified during the recent 2008 eruption of Chaitén volcano in Chile (Watt et al., 2009). Late on August 13, 1991 a northwesterly wind was established that wandered very little during the rest of the event. For the remainder of the phase II eruption (events 3 and 4) the plume direction was approximately fixed in a southeasterly direction and this is reflected in the relatively simple, coarse-grained nature of the rest of the deposit (e.g., localities 28, 29, and 30).

4.2. Lithic isopleth data and calculated column heights

The model of Carey and Sparks (1986) infers eruption column heights from the size of lithic clasts and the crosswind distance of an isopleth (perpendicular to the main dispersal axis), which is a function of the eruption column height. This model has been applied to the 1980 eruption at Mt. St. Helens and is in good agreement with the available radar-estimated column heights (e.g., Carey et al., 1980). The maximum lithic data from phase II of the 1991 eruption of Hudson volcano has been used to create isopleth maps for each of the correlated fall units of the paroxysmal eruption sequence (Fig. 11). From these isopleths the maximum column heights have been

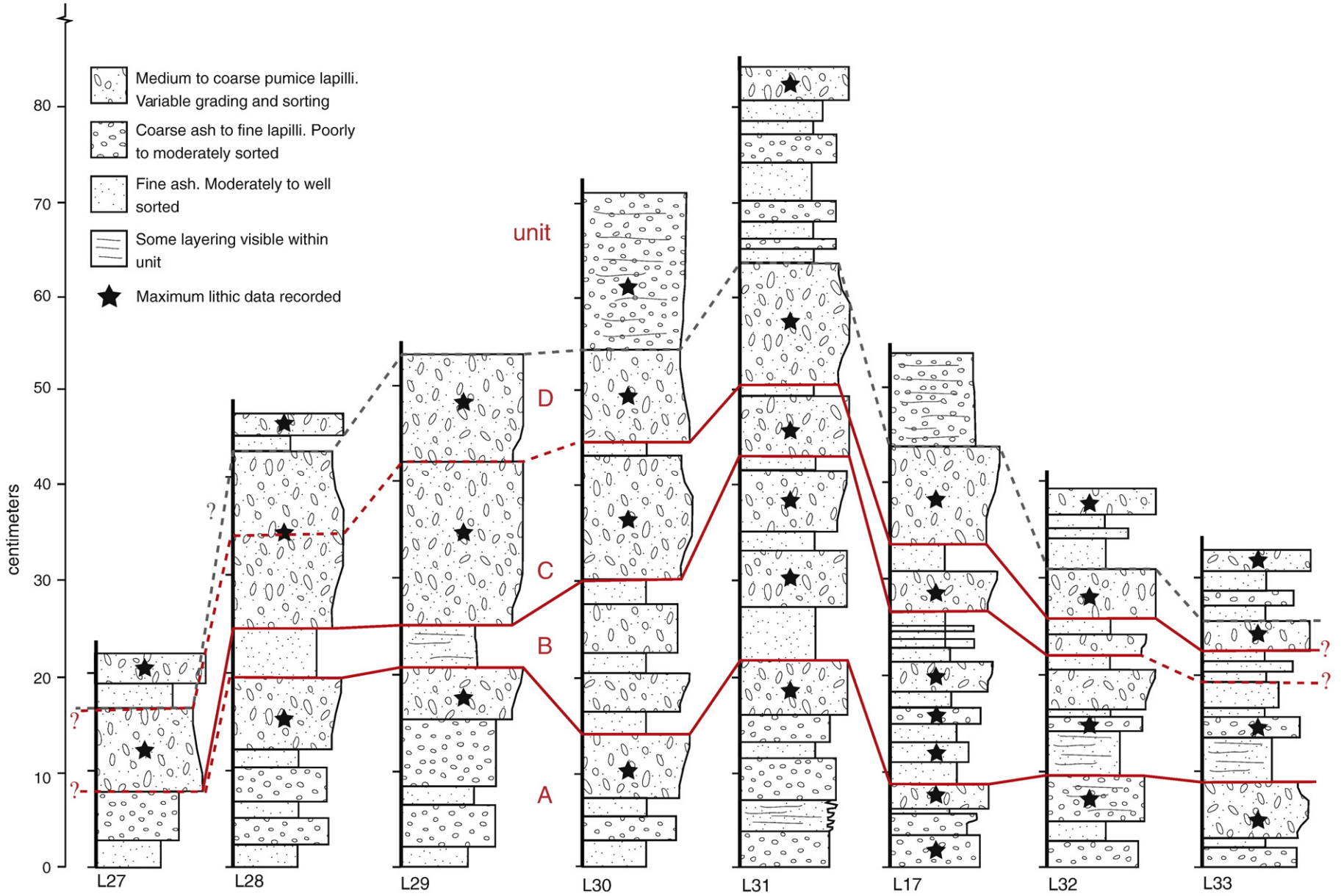

Fig. 10. Stratigraphy of the 1991 phase II fall deposit. The sample locations are approximately perpendicular to the main dispersal axis (see Fig. 1 inset). Correlations between units (A–D) have been made based on similarities in deposit characteristics (see text). Black stars denote sampling point for maximum lithic and pumice data. Dashed lines represent potential correlations.

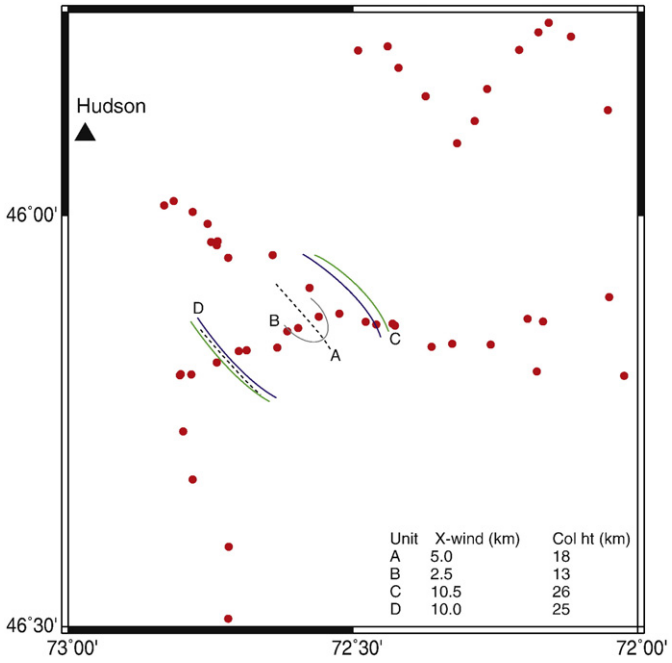

Fig. 11. Isopleth boundaries for the correlated units (refer Fig. 10). Units C and D have similar crosswind distances and therefore similar column heights (refer Table 3). Filled black circles are sampling locations.

calculated following the methods of Carey and Sparks (1986) and for the most part, the calculated column heights are greater than the observations reported (Table 3).

The observed column height estimations for events 2 (August 12–13) and 3 (August 13–14) are aircraft-based (e.g., Naranjo et al., 1993) and considered reliable for the times of observation. However, it may be that the observations of maximum column height during events 2 and 3 never recorded the peak height. The reported column heights represent only one observation for sequences that each lasted for at least 20 h. Given that both simulated (e.g., Suzuki and Koyaguchi, 2009) and observed (Harris et al., 1981; Holasek et al., 1996a) eruption column heights can fluctuate even under steady state conditions, the probability of observing the peak height during these events is thus quite low given the variations recorded by continuous column height monitoring during other plinian eruptions.

Bad weather conditions combined with a nighttime eruption made visual estimation of the column height of event 4 (August 14–15) difficult. The column height (i.e., 17–18 km) reported for this event is a temperature-based estimate (Bulletin of the Global Volcanism Network [BGVN], 1991) and the infrared image used in the BGVN report (i.e., Fig. 3 in BGVN report 16:07) was captured 12 h after the start of this 15-hour event. The estimated column height may thus reflect the atmospheric altitude at which the plume was dispersed and not the maximum height achieved during the peak of the eruption.

Variations in dispersal axis orientation due to shifting wind directions could produce a wider deposit than would result from a plume of similar column height with a fixed direction. The resultant isopleth maps could have an expanded crosswind dimension that would return overestimated eruption column heights based on the method of Carey and Sparks (1986). Widening of the deposit isopleths by a "wandering plume" may explain the overestimations in column height for unit A (event 2 August 12–13), but it does not account for the higher than observed heights for the final event of the phase II eruption. The calculated column heights for units B, C and D are 13, 26 and 25 km respectively (Table 3). If we assume units C and D are related to event 4 (August 14–15), then the maximum lithic-based column heights (25–26 km) are ~40% higher than the current accepted height (17–18 km). The lithic-based height estimations for units C and D (26 and 25 km) may reflect the maximum column height reached by the central portion of the column as it ascends beyond the level of neutral buoyancy due to excess momentum, whereas the aircraft and temperature based estimates are a measure of the height of the laterally spreading umbrella cloud (17–18 km).

Isopleth maps of fall deposits also provide information about the intensity of the prevailing winds during transport and deposition. Fig. 12 compares the field data from the 1991 phase II eruption of Hudson volcano to the results from the theoretical model of Carey and Sparks (1986). Most historical eruptions define circular to elliptical shaped isopleths. The phase II eruptions of Hudson volcano exhibit evidence of very strong winds producing isopleths with an anomalous elongated and narrow pattern. The wind velocity, based on the dispersal of the lithic clasts, can be estimated from Fig. 12 and compared to the values from the NCEP reanalysis data set. Data from the correlated units of the Hudson phase II eruptions define a curvilinear trend of increasing downwind range with increasing crosswind range (Fig. 12). Extrapolation of the calculated wind speeds (Carey and Sparks, 1986) suggests velocities close to 70 ms^{-1} for the Hudson phase II eruptions, values similar to results from the reanalysis wind field at between 20 and 25 km altitude (e.g., Fig. 3). It should be noted however, that the wind speeds of the Carey and Sparks (1986) model represent peak values of an idealized profile with maximum wind speeds at the tropopause. Below the tropopause winds decrease to zero at ground level and above the tropopause they decrease linearly to approximately 16 km and remain constant above this level (figure 11 of Carey and Sparks, 1986). Actual wind profiles that have less steeply decreasing velocity gradients above and below the tropopause would yield model curves displaced to the right (Fig. 12). Thus a profile with a peak value of 50 ms^{-1} near the tropopause (Fig. 3) could potentially produce the highly elongated isopleths observed for the 1991 Hudson fall deposits. In any event, the Hudson isopleth distributions represent the most highly elongated geometries of any documented fall deposits.

Table 3
Observed and calculated eruption column heights from the 1991 Hudson eruption.

Date	Phase	Observed column height[a]	Subunit	Event	Crosswind range (km)	Downwind range (km)	Estimated column height (km)[b]
8-Aug	PI	7–12 km	–	n.a.	–	–	–
12-Aug	PII	12 km	A	2	5.0	~40	~18
13-Aug	PII	15 km	B	3	2.5	~38	~13
14-Aug	PII	18 km	C	4[c]	10.5	~48	~26
15-Aug	PII	–	D	4	10.0	~41	~25

[a] Data from Naranjo et al. (1993); Constantine et al. (2000).
[b] Following the methods of Carey and Sparks (1986).
[c] Correlated to event 4 based on the estimated column height and deposit characteristics.

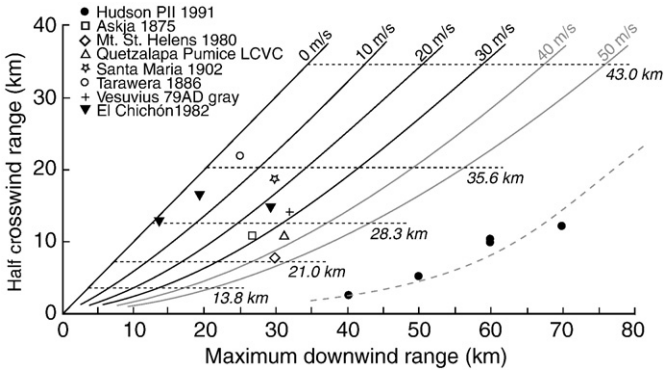

Fig. 12. Crosswind half-width versus the maximum downwind range of the 0.8 cm diameter lithic clasts. Data points from Sigurdsson et al. (1985), Carey and Sparks (1986), Carey and Sigurdsson (1986), Rodríguez et al. (2002), and this study. Eruption column heights (dashed black line) and 0–30 ms^{-1} wind speed contours (solid black lines) from Carey and Sparks (1986). 40 and 50 ms^{-1} contours (solid gray line) extrapolated from Carey and Sparks (1986). Gray dashed line represents the wind speed defined by the Hudson data. Multiple data points (i.e., Hudson and El Chichón) represent correlated subunits within the overall deposit.

5. Discussion

5.1. Levels of tephra transport

PUFF simulations of the 1991 explosive eruptions of Hudson volcano can successfully reproduce the aerial distribution and temporal evolution of the downwind plumes as recorded by satellite imagery. The aerial extent of the simulated plumes from both phases of the eruption also shows good correlation to the isopachs that define the mapped fall deposits. An animation of the simulated plume from the 1991 eruption of Hudson volcano shows the evolution of the modeled ash cloud (see Supplementary animations). However, there appears to be a discrepancy between the observed column heights and the optimal level of ash transport in the simulations. The height of an eruption column (H_T) reflects the maximum altitude reached as the column ascends primarily due to buoyancy. The column then spreads laterally in the region between H_T and H_B, the level where the density of the atmosphere and the cloud are equal (level of neutral buoyancy), forming the umbrella cloud (Sparks, 1986). There is a tendency for the central portion of the eruption column to ascend beyond the level of neutral buoyancy as a result of excess momentum, and the density difference between the column and the atmosphere results in subsidence of this portion of the plume (Sparks, 1986; Woods, 1988). The PUFF simulation parameters were selected to best match the satellite data when reproducing the distribution and evolution of the downwind plume and thus reflect the long-range distal transport of the fine ash component. As such, the optimal altitude for ash transport may not correlate with the maximum column height at the source but, instead lie, at or slightly above the base of the umbrella cloud as it evolves into a distal transport regime (e.g., Koyaguchi, 1996; Suzuki and Koyaguchi, 2009; Fero et al., 2009). The level of neutral buoyancy for the 12, 15, and 18-km-high phase II eruption columns have been calculated at 9.0, 11.3, and 13.6 km respectively (following the methods of Sparks, 1986) and coincide generally with the level of the tropopause (11–14 km).

The maximum column height and the point of injection of the highest ash concentration (i.e., z-width) exert the strongest controls on plume position in the PUFF simulations. This is most evident in the position of the plume from event 4 of phase II (Fig. 8). The best matches to the satellite-inferred plume outlines are achieved through varying the z-width value such that injection of the majority of ash particles occurs at or around the tropopause (level of neutral buoyancy). A similar range in altitude for optimal transport of the 1991 SO_2 cloud has been previously noted (e.g., Schoeberl et al., 1993); thus, the level of dominant ash transport (i.e., ~11 km) during the 1991 eruptions is inferred to be lower than the maximum recorded column heights (13–18 km). Differences between maximum column height and the level of principal ash transport have also been reported for other recent eruptions (El Chichón 1982 [Matson, 1984]; Mt. St. Helens 1980 [Fero et al., 2008]; Pinatubo 1991 [Koyaguchi and Ohno, 2001; Fero et al., 2009]). Combined subsidence of the central portion of the eruption column (e.g., Sparks, 1986) and the laterally spreading component of the umbrella region (e.g., Holasek et al., 1996b) could result in lowering of the level of principal transport for the majority of ash (Fig. 13). Settling of the laterally spreading umbrella region has also been suggested for the 1991 eruption at Pinatubo as a mechanism for concentrating the majority of ash particles to levels much lower than the maximum observed eruption column height (e.g., Koyaguchi and Ohno, 2001; Fero et al., 2009).

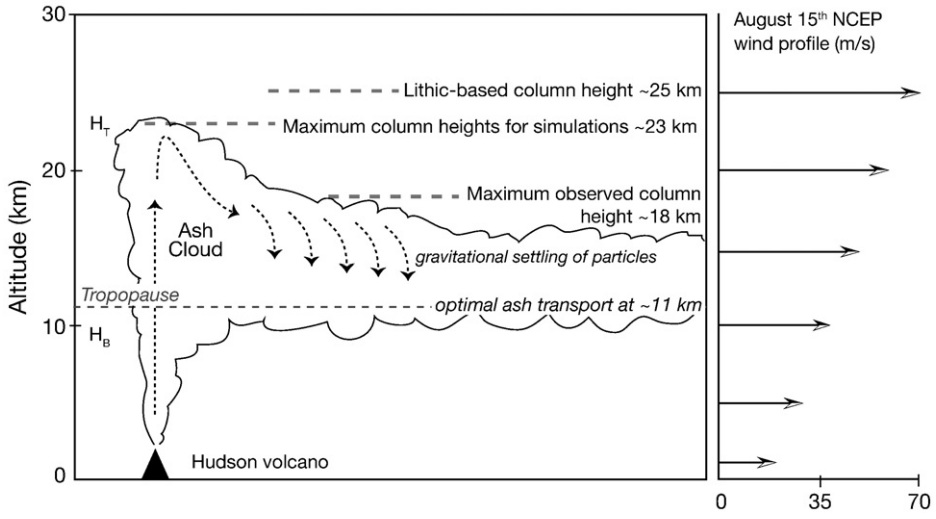

Fig. 13. Schematic representation of the plume associated with event 4 (August 14–15) of the phase II eruption. The eruption occurred in a strong wind field (~50 ms^{-1}) and gravitational settling results in the concentration of the ash particles at the tropopause. The observed column height for this event (17–18 km) represents the altitude at which the laterally spreading portion of the plume is transported and may not reflect the maximum height reached during the event. The maximum column height (23–25 km) is recorded by the lithic-based estimation. H_T: maximum column height. H_B: neutral buoyancy level.

5.2. Multilayered fall deposit stratigraphy

Layering and grain size variations within tephra fall deposits have been largely attributed to changes in eruptive style, discrete events, or changes in eruption column height during explosive eruptive sequences (e.g., Walker, 1981; Carey and Sigurdsson, 1987; Scasso et al., 1994). For sequences that occur over relatively long periods (i.e., days to weeks) a fluctuating wind direction may also contribute significantly to the internal stratigraphic complexity of fall deposits. At Hudson volcano, simulations of the 1991 eruptions have revealed major shifts in wind direction, on time-scales of a single day, occurring during some of the eruptive events. Some of the stratigraphic complexity of the 1991 phase II fall deposit (unit A) could have resulted from the shifting wind direction that occurred during the initial stages of the paroxysmal phase (event 2 August 12–13). Repeated crossing of the main dispersal axis of the deposit by a "wandering plume" could promote the deposition of alternating ash and pumice lapilli, as a result of cross-plume variations in grain size and differential transport of tephra at lower altitudes (e.g., Mt. St. Helens [Sarna-Wojcicki et al., 1981]).

The multilayered fall deposit from phase II of the 1991 explosive eruption exposes potential problems in inferring eruption column height from such complex distributions of maximum lithic and pumice clasts. In general, the isopleth-based column height estimations are higher than those recorded during the eruption (Table 3). One possible explanation involves changing atmospheric conditions (e.g., wind direction) and subsequent plume movement during an eruption. This may contribute to overestimations of column heights by widening the isopleth crosswind distance. Models used to infer paleovolcanological parameters from deposit characteristics (e.g., Carey and Sparks, 1986) could potentially overestimate column heights for continuous eruptions or eruptive events that occur during a period with significant changes in wind direction. The "wandering plume" of event 2 during the phase II eruption (August 12–13) has widened the cross-axis dimension of the fall deposit and may explain the discrepancies between the observed and estimated column heights for unit A (~12 versus 18 km). However, this does not explain the overestimations from the latter stage of the eruption (phase II event 4) when the plume direction was relatively constant in a southeasterly direction. One possible explanation for this discrepancy is that the lithic-based estimation of event 4 (phase II) reflects the maximum column height reached as the central portion of the column ascends beyond the level of neutral buoyancy due to excess momentum. Whereas, the temperature-based column height estimation reflects the lower altitude the plume attains after the laterally spreading portion of the umbrella region subsides due to gravitational settling of ash particles (Fig. 13). The PUFF simulations suggest that eruption column heights similar to the lithic-based estimates can be employed to successfully replicate the aerial distribution of the plume associated with the latter stages of the phase II eruption (e.g., Fig. 9) but only if the principal levels of ash transport are at or near the tropopause.

6. Conclusions

PUFF modeling of the 1991 explosive eruptions of Hudson volcano, Chile, can successfully reproduce the aerial distribution and evolution of the ash plumes from both phases of the eruption as defined by satellite images of the activity. Several important implications for the dispersal of plumes and the subsequent distal fall deposits from explosive eruptions released into strong winds have been identified during the course of these simulations.

First, variations in eruption column height and the zone of maximum ash concentration (i.e., the z-width) display the strongest influence on plume shape and evolution. The optimal agreement between simulated and observed plumes occurs when ash is concentrated at or around the tropopause (~11 km). This height is lower than both the maximum observed and lithic-calculated column heights (e.g., Table 3), but coincides with the estimated neutral buoyancy level of the eruption column's umbrella region. Several combinations of column height and z-width can result in good matches between simulated and observed plume dispersal. However, eruption columns in excess of 25 km require excessively large z-widths and begin to deviate from the principal ash transport directions identified in satellite imagery. The concentration and subsequent long-range transport of ash at the tropopause are likely to result from gravitational settling of particles within the laterally spreading portion of the umbrella region (e.g., Pinatubo [Koyaguchi and Ohno, 2001; Fero et al., 2009]).

Second, stratigraphic complexity within fall deposits in general may arise from a "wandering plume" that repeatedly crosses the main dispersal axis as documented in this study for some of the paroxysmal phase of the Hudson eruption. The grain size being deposited from a continuous eruption could change from ash to pumice lapilli as a result of differential transport of tephra at varying altitudes (e.g., Mt. St. Helens [Sarna-Wojcicki et al., 1981]). Such a change in depositional regime is likely to have contributed to the multilayered deposit composed of alternating fine and coarse units at the base of the 1991 Hudson fall stratigraphy.

Third, models employed to estimate maximum eruption column heights from deposit characteristics such as clast distribution patterns, could return overestimated values if the eruption occurred in a highly variable wind field and crosswind isopleths widths were widened due to a plume that wandered across the main depositional axis. Extensive analysis of detailed stratigraphic data to identify individual units, traceable over large distances, is thus a critical prerequisite before applying model-based techniques for paleovolcanological reconstructions of pyroclastic fall deposits.

Acknowledgments

The authors thank A Bande for assistance during fieldwork, MG Kratzmann for georeferencing support, and JT Merrill for atmospheric expertise. The manuscript benefited from reviews by T Koyaguchi and PW Webley. This research was supported by NSF grant EAR-0337023 to SNC and CONICET grant to RAS. JAN acknowledges Fondecyt Project 1960186 and Sernageomin's Volcanic Hazard Programme.

Appendix A. Supplementary data

Supplementary data associated with this article can be found, in the online version, at doi:10.1016/j.jvolgeores.2009.11.021.

References

Aloisi, M., D'Agostino, M., Dean, K.G., Mostaccio, A., Neri, G., 2002. Satellite analysis and PUFF simulation of the eruptive cloud generated by the Mount Etna paroxysm of 22 July 1998. J. Geophys. Res. 107 (B12), 2373.

Bitschene, P.R., Fernandez, M.I., 1995. Volcanology and petrology of fallout ashes from the August 1991 eruption of the Hudson Volcano (Patagonian Andes). In: Bitschene, P., Medina, J. (Eds.), The August 1991 eruption of the Hudson Volcano (Patagonian Andes); a thousand days after. Cuvillier, Gottingen, pp. 27–54.

Bulletin of the Global Volcanism Network Smithsonian Institute, Washington DC, 16 (7), (1991), 2–4.

Carey, S., Sigurdsson, H., 1986. The 1982 eruptions of El Chichón volcano, Mexico (2): Observations and numerical modelling of tephra-fall distribution. Bull. Volcanol. 48 (2–3), 127–141.

Carey, S., Sigurdsson, H., 1987. Temporal variations in column height and magma discharge rate during the 79 A.D. eruption of Vesuvius. Geol. Soc. Am. Bull. 99, 303–314.

Carey, S., Sparks, R.S.J., 1986. Quantitative models of the fallout and dispersal of tephra from volcanic eruption columns. Bull. Volcanol. 48, 109–125.

Carey, S., Sigurdsson, H., Gardner, J.E., Criswell, W., 1990. Variations in column height and magma discharge during the May 18, 1980 Eruption of Mount St. Helens. J. Volcanol. Geotherm. Res. 43, 99–112.

Constantine, E.K., Bluth, G.J.S., Rose, W.I., 2000. TOMS and AVHRR Observations of Drifting Volcanic Clouds From the August 1991 Eruptions of Cerro Hudson. In:

Mouginis-Mark, P., Crisp, J.A., Fink, J.H. (Eds.), Remote Sensing of Active Volcanism. Geophysical Monograph, Washington, DC, pp. 45–64.
Doiron, S.D., Bluth, G.J.S., Schneltzer, C.C., Krueger, A.J., Walter, L.S., 1991. Transport of the Cerro Hudson SO_2 clouds. EOS Trans. AGU 72 (45), 489.
Fero, J., Carey, S.N., Merrill, J.T., 2008. Simulation of the 1980 eruption of Mount St. Helens using the ash-tracking model PUFF. J. Volcanol. Geotherm. Res. 175 (3), 355–366.
Fero, J., Carey, S.N., Merrill, J.T., 2009. Simulating the dispersal of tephra from the 1991 Pinatubo eruption: implications for the formation of widespread ash layers. J. Volcanol. Geotherm. Res. 186 (1–2), 120–131.
Gutierrez, F., Gioncada, A., Gonzalez-Ferran, O., Lahsen, A., Mazzuoli, R., 2005. The Hudson Volcano and surrounding monogenetic centres (Chilean Patagonia): an example of volcanism associated with ridge-trench collision environment. J. Volcanol. Geotherm. Res. 145, 207–233.
Haberle, S.G., Lumley, S.H., 1998. Age and origin of tephras recorded in postglacial lake sediments to the west of the southern Andes, 44°S to 47°S. J. Volcanol. Geotherm. Res. 84 (3–4), 239–256.
Harris, D.M., Rose, W.I., Roe, R., Thompson, M.R., 1981. Radar observations of ash eruptions. In: Lipman, P.W., Mullineaux, D.R. (Eds.), The 1980 eruptions of Mount St. Helens, Washington: USGS Professional Paper, vol. 1250, pp. 323–334.
Holasek, R.E., Rose, W.I., 1983. Demonstration of use of digital satellite AVHRR images for eruption cloud mapping. Bull. - N. M. Bur. Geol. Miner. Resour. Rep. 131, 133.
Holasek, R.E., Self, S., Woods, A.W., 1996a. Satellite observations and interpretation of the 1991 Mount Pinatubo eruption plumes. J. Geophys. Res. 101 (B12), 27,635–27,655.
Holasek, R.E., Woods, A.W., Self, S., 1996b. Experiments on gas–ash separation processes in volcanic umbrella plumes. J. Volcanol. Geotherm. Res. 70 (3–4), 169–181.
Kalnay, E., Kanamitsu, M., Kistler, R., et al., 1996. The NCEP/NCAR 40-year reanalysis project. Bull. Am. Meteorol. Soc. 77 (3), 437–470.
Kilian, R., Behrmann, J.H., 2003. Geochemical constraints on the sources of Southern Chile Trench sediments and their recycling in arc magmas of the Southern Andes. J. Geol. Soc. 160, 57–70.
Koyaguchi, T., 1996. Volume estimation of tephra-fall deposits from the June 15, 1991, eruption of Mount Pinatubo by theoretical and geological methods. In: Newhall, C.G., Punongbayan, R.S. (Eds.), Fire and Mud. Eruptions and Lahars of Mount Pinatubo, Philippines. Philippine Institute of Volcanology and Seismology, Quezon City and University of Washington Press, Seattle and London, pp. 583–600.
Koyaguchi, T., Ohno, M., 2001. Reconstruction of eruption column dynamics on the basis of grain size of tephra fall deposits 2. Application to the Pinatubo 1991 eruption. J. Geophys. Res. 106 (B4), 6513–6533.
Krueger, A.J., Walter, L.S., Bhartia, P.K., Schnetzler, C.C., Krotkov, N.A., Sprod, I., Bluth, G.J.S., 1995. Volcanic sulfur dioxide measurements from the Total Ozone Mapping Spectrometer (TOMS) instruments. J. Geophys. Res. 100, 14057–14076.
Matson, M., 1984. The 1982 El Chichón Volcano eruptions — a satellite perspective. J. Volcanol. Geotherm. Res. 23 (1–2), 1–10.
Naranjo, J.A., Stern, C.R., 1998. Holocene explosive activity of Hudson Volcano, southern Andes. Bull. Volcanol. 59, 291–306.
Naranjo, J.A., Moreno, H., Banks, N., 1993. La erupción del Volcán Hudson en 1991 (46° S), Región XI, Aisén. Chile Boletin 44, 1–50.
Oppenheimer, C., 1998. Volcanological applications of meteorological satellites. Int. J. Remote Sens. 19 (15), 2829–2864.
Prata, A.J., 1989a. Infrared radiative transfer calculations for volcanic ash clouds. Geophys. Res. Lett. 16, 1293–1296.
Prata, A.J., 1989b. Observations of volcanic ash clouds in the 10–12 Am window using AVHRR/2 data. Int. J. Remote Sens. 10, 751–761.
Rodríguez, S.-R., Siebe, C., Komorowski, J.-C., Abrams, M., 2002. The Quetzalapa Pumice: a voluminous late Pleistocene rhyolite deposit in the eastern Trans-Mexican Volcanic Belt. J. Volcanol. Geotherm. Res. 113 (1–2), 177–212.
Rose, W.I., 2003. Advancing remote sensing of volcanic clouds. EOS Trans. AGU 84, 351.
Rose, W.I., Bluth, G.J.S., Ernst, G.G.J., 2000. Integrating retrievals of volcanic cloud characteristics from satellite remote sensors: a summary. Philos. Trans. R. Soc. Lond. 358, 1585–1606.
Sarna-Wojcicki, A.M., Shipley, S., Waitt Jr., R.B., Dzurisin, D., Wood, S.H., 1981. Areal distribution, thickness, mass, volume, and grain size of air-fall ash from the six major eruptions of 1980. In: Lipman, P.W., Mullineaux, D.R. (Eds.), The 1980 eruptions of Mount St. Helens, Washington: USGS Professional Paper, vol. 1250, pp. 577–600.
Scasso, R.A., Carey, S., 2005. Morphology and formation of glassy volcanic ash from the August 12–15, 1991 eruption of Hudson Volcano, Chile. Lat. Am. J. Sedimentol. Basin Anal. 12 (1), 3–21.
Scasso, R.A., Corbella, H., Tiberi, P., 1994. Sedimentological analysis of the tephra from the 12–15 August 1991 eruption of Hudson volcano. Bull. Volcanol. 56, 121–132.
Schoeberl, M.R., Doiron, S.D., Lait, L.R., Newman, P.A., Krueger, A.J., 1993. A simulation of the Cerro Hudson SO_2 cloud. J. Geophys. Res. 98 (D2), 2949–2955.
Searcy, C., Dean, K., Stringer, W., 1988. PUFF: a high-resolution volcanic ash tracking model. J. Volcanol. Geotherm. Res. 80, 1–16.
Sigurdsson, H., Carey, S., Cornell, W., Pescatore, T., 1985. The eruption of Vesuvius in 79 A.D. Res. Explor. 1, 332–387.
Simpson, J.J., Hufford, G., Pieri, D., Berg, J., 2000. Failures in detecting volcanic ash from a satellite-based technique. Remote Sens. Environ. 72, 191–217.
Sparks, R.S.J., 1986. The dimensions and dynamics of volcanic eruption columns. Bull. Volcanol. 48, 3–15.
Stern, C.R., 1991. Mid-Holocene tephra on Tierra del Fuego (54° S) derived from the Hudson Volcano (46° S): evidence for a large explosive eruption. Rev. Geol. Chile 18 (2), 139–146.
Suzuki, Y.J., Koyaguchi, T., 2009. A three-dimensional numerical simulation of spreading umbrella clouds. J. Geophys. Res. 114, B03209. doi:10.1029/2007JB005369.
Tupper, A., Carn, S., Davey, J., Kamada, Y., Potts, R., Prata, F., Tokuno, M., 2004. An evaluation of volcanic cloud detection techniques during recent significant eruptions in the western 'Ring of Fire'. Remote Sens. Environ. 91 (1), 27–46.
Walker, G.P.L., 1981. Plinian eruptions and their deposits. Bull. Volcanol. 44, 223–240.
Watt, S.F.L., Pyle, D.M., Mather, T., Martin, R.S., Matthews, N.E., 2009. Fallout of volcanic ash from the May 2008 explosive eruption of Chaitén, Chile. J. Geophys. Res. 114, B04207. doi:10.1029/2008JB006219.
Webley, P.W., Stunder, B.J.B., Dean, K.G., 2009. Preliminary sensitivity study of eruption source parameters for operational volcanic ash cloud transport and dispersion models — a case study of the August 1992 eruption of the Crater Peak vent, Mount Spurr, Alaska. J. Volcanol. Geotherm. Res. 186 (1–2), 108–119.
Wessel, P., Smith, W.H.F., 1991. Free software helps map and display data. EOS Trans. AGU 72 (41), 441–448.
Woods, A.W., 1988. The fluid dynamics and thermodynamics of eruption columns. Bull. Volcanol. 50, 169–193.
Woods, A.W., Self, S., 1992. Thermal disequilibrium at the top of volcanic clouds and its effect on estimates of the column height. Nature 355, 628–630.